2013

Stability and power optimality in time-periodic flapping wing structures

Bret Stanford
Wright-Patterson AFB, bretkennedystanford@gmail.com

Philip Beran
Wright-Patterson AFB

Richard Snyder
Wright-Patterson AFB

Mayuresh Patil
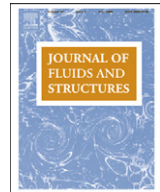*Virginia Polytechnic and State University*

Stability and power optimality in time-periodic flapping wing structures

Bret Stanford [a,*], Philip Beran [a], Richard Snyder [a], Mayuresh Patil [b]

[a] U.S. Air Force Research Laboratory, Wright-Patterson AFB, Dayton, OH 45433, USA
[b] Virginia Polytechnic and State University, Blacksburg, VA 24061, USA

ABSTRACT

This paper investigates the nonlinear dynamics of a vehicle with two flexible flapping wings. The body dynamics and the wings' deformation are monolithically grouped into a single system of equations, with aerodynamics accounted for by a quasi-steady blade element method. A periodic shooting method is then used to locate closed orbits of this non-autonomous system, and Floquet multipliers assess the linearized stability about the nonlinear orbit. This framework is then exposed to a gradient based optimizer, in order to quantify the role of wing planform variables, wing structure variables, and kinematic actuation variables in obtaining vehicles with superior open-loop stability characteristics, and/or low-power requirements.

Published by Elsevier Ltd.

1. Introduction

A recent work by the authors (Stanford et al., 2012) has studied the power-optimal aeroelastic response of a flexible flapping wing in hover. The wing itself is modeled as a geometrically-nonlinear beam structure, and quasi-steady airloads are computed using a blade-element method. Parameterizing the wing's shape and stiffness distribution (as a function of the spanwise location along the wing), as well as the kinematics used to actuate the wing, the peak power requirements were minimized using gradient-based optimization, subject to an aerodynamic lift-generation constraint and a series of stress-based failure constraints. The results demonstrate that substantial decreases in the peak power requirements are available by properly phasing the energy flow between the inertial kinetic energy rate, the elastic strain energy rate, and the aerodynamic losses. Optimal tailoring of these energy transfer mechanisms for flapping wings is discussed in great detail by Tantanawat and Kota (2007).

One deficiency of the framework outlined by Stanford et al. (2012) is the assumption that the root of the wing is pinned in space, and the flapping kinematics are realized by rotations about this fixed joint. Such an assumption mimics the set-up commonly found in bench-top experiments (for example, Wu et al. (2010)), but an actual flapping wing MAV may show relevant interactions between the flight dynamics of a body and the aeroelastic behavior of the flapping wings. The goal of this work is to discuss numerical methods by which these interactions may be captured, quantify the stability of the resulting time-periodic system, and introduce these metrics into the optimization process.

If the wing joints of two (or potentially more) flapping wings are attached to an inertial body (fuselage) which is free to translate and rotate in space, several interesting interactions can occur. The flight dynamics of the body will react to the unsteady inertial and aerodynamic loads generated by the flapping wings in a nonlinear manner: derivations of these

---

equations of motion can be found in work by Sun et al. (2007) and Orlowski and Girard (2011). The motion of the wings relative to the body is wholly prescribed by the kinematics in this work, but the absolute motion of the wings is a combination of the kinematics and the body motion. The inertial and aerodynamic loads generated by the wings are thus altered, closing a feedback loop between the wings and the body. If the wings are considered to be flexible as well, a strongly-coupled three-field dynamics problem results: body dynamics, wing deformation, and wing aerodynamics (fluidic state). The aerodynamic modeling used here (Berman and Wang, 2007) is quasi-steady, and so the aerodynamic terms can be projected onto the rigid and deformational dynamics states, but this will not be possible for higher-fidelity unsteady fluids tools (e.g. Navier–Stokes). Examples of flight dynamics analysis with flexible flapping wings are given by Richter and Patil (2010) and by Su and Cesnik (2011).

A periodic shooting method can be used to locate a closed time-periodic orbit of the non-autonomous system (the flapping frequency, like the kinematics, is prescribed here). This entails forcing the system state (which, in general, will be a monolithic vector containing the aerodynamic, structural, and body motion unknowns, as well as their time derivatives) as computed at the end of a flapping cycle to coincide with the prescribed state at the beginning. The general technique is described by Nayfeh and Balachandran (1995), where a time integration scheme connects the beginning and end of the flapping cycle, and the required derivative of the latter state with respect to the former is the monodromy matrix, or state-transition matrix (Johnson, 1980). The eigenvalues of this matrix are the Floquet multipliers: if each multiplier lies within the unit circle, the system is stable. Here stability implies that perturbations to the trimmed orbit at the beginning of a flapping cycle will have been found to decay at the end of the cycle, and the flight motion gradually returns to the trimmed time-periodic orbit (Nayfeh and Balachandran, 1995).

Floquet analysis of bodies with flapping wings is considered by Bierling and Patil (2009), Dietl and Garcia (2008), Rosenfeld and Wereley (2009), Richter and Patil (2010), and Bolender (2010), where the motion is typically found to be unstable in an open-loop sense. As the multipliers quantify the stability of the system, they can be introduced into a design-optimization setting, in order to draw relationships between various design parameters and the resulting stability. Optimization of Floquet multipliers has been considered by Seyranian et al. (2000) for generic structural systems, Celi (1999) for rotorcraft, and by the authors (Stanford et al., in press) specifically for flapping wing flight dynamics. This latter work is limited to rigid wings and kinematic design variables: wing flexibility and a greater variety of design variables are the contribution of the current work.

It should finally be noted that the process of applying design optimization to a flapping wing system in order to improve its open-loop stability (by pushing each Floquet multiplier towards the unit circle) is not meant to replace the eventual inclusion of a closed-loop controller. This work is meant to ascertain the degree to which orbital stability is affected during the design process, and demonstrate conflicts that arise between this stability and input power requirements to sustain flight. Open-loop stability may be obtained, in some cases, using the techniques discussed below, but the resulting system is unable to hold a position (station-keeping) in the presence of any disturbance, or maintain stability at all when the disturbance is very strong (Stanford et al., in press). Closed-loop control of a general flapping system can be obtained (see Oppenheimer et al. (2010), for example), and it is expected that a feedback controller can be included for the specific system used here as well, where linearization occurs about an entire nonlinear orbit (Floquet multiplier) obtained via a shooting method.

2. Equations of motion

The vehicle under consideration in this work (seen in Fig. 1) operates within a fixed inertial coordinate system $(x_i - y_i - z_i)$. A second coordinate system is attached to the center of gravity of a rigid fuselage body ($x_b - y_b - z_b$, located at point B), and a third coordinate system ($x_w - y_w - z_w$) is located at the hinge point H. This wing system rotates with respect to the body as dictated by the commanded kinematics, and specifies the location of the *un-deformed* wing. The flexible wing deforms within this system, and is assumed to be clamped at the root (point H).
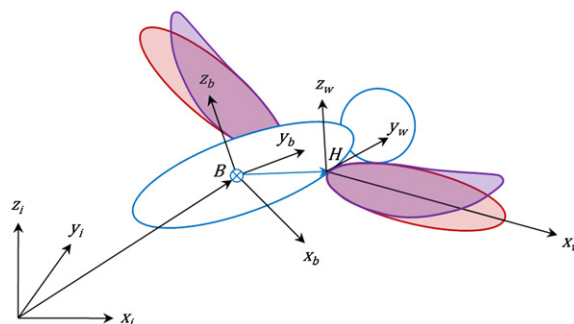

Fig. 1. Body and flapping wing coordinate systems.

The attitude and position of the body is defined by

$$\boldsymbol{\varphi}^B = \{\psi^B \quad \Theta^B \quad \Phi^B\}^T, \quad {}_i\boldsymbol{r}^B = \{{}_ix^B \quad {}_iy^B \quad {}_iz^B\}^T, \tag{1}$$

where the susbscript (i) indicates that the term is written in the inertial coordinate system, and $\boldsymbol{\varphi}^B$ is a collection of three Euler angles. The angular velocity of the body, written in the body frame, is

$$
{}_b\boldsymbol{\omega}^B = \begin{bmatrix} \cos(\Theta^B)\cos(\Phi^B) & \sin(\Phi^B) & 0 \\ -\cos(\Theta^B)\sin(\Phi^B) & \cos(\Phi^B) & 0 \\ \sin(\Theta^B) & 0 & 1 \end{bmatrix} \cdot \begin{Bmatrix} \dot{\Psi}^B \\ \dot{\Theta}^B \\ \dot{\Phi}^B \end{Bmatrix} = \boldsymbol{E}_{bi} \cdot \dot{\boldsymbol{\varphi}}^B. \tag{2}
$$

The transformation matrix between the inertial frame and the body frame is given by

$$
\boldsymbol{T}_{bi} = \begin{bmatrix} 1 & 0 & 0 \\ 0 & \cos(\Psi^B) & -\sin(\Psi^B) \\ 0 & \sin(\Psi^B) & \cos(\Psi^B) \end{bmatrix} \cdot \begin{bmatrix} \cos(\Theta^B) & 0 & \sin(\Theta^B) \\ 0 & 1 & 0 \\ -\sin(\Theta^B) & 0 & \cos(\Theta^B) \end{bmatrix} \cdot \begin{bmatrix} \cos(\Phi^B) & -\sin(\Phi^B) & 0 \\ \sin(\Phi^B) & \cos(\Phi^B) & 0 \\ 0 & 0 & 1 \end{bmatrix}. \tag{3}
$$

The velocity of the body is then written as

$$
{}_i\dot{\boldsymbol{r}}^B = \left\{ {}_i\dot{x}^B \quad {}_i\dot{y}^B \quad {}_i\dot{z}^B \right\}^T = {}_i\boldsymbol{v}^B = \boldsymbol{T}_{bi} \cdot {}_b\boldsymbol{v}^B, \tag{4}
$$

where ${}_b\boldsymbol{v}^B$ is the velocity written in the body-attached coordinate system. The acceleration of the body is given as

$$
{}_i\dot{\boldsymbol{v}}^B = \boldsymbol{T}_{bi} \cdot {}_b\tilde{\boldsymbol{\omega}}^B \cdot {}_b\boldsymbol{v}^B + \boldsymbol{T}_{bi} \cdot {}_b\dot{\boldsymbol{v}}^B, \tag{5}
$$

where the tilde operator indicates a skew-symmetric matrix.

The prescribed flapping kinematics of the wing (i.e., attitude of the un-deformed wing with respect to the body) are governed by three Euler angles $\boldsymbol{\varphi}^W = \left\{ \phi^W \quad \theta^W \quad \eta^W \right\}^T$, where ϕ^W is the azimuthal stroke plane motion, θ^W is the out-of-stroke plane deviation, and η^W is the wing rotation (feathering). The angular velocity of the un-deformed wing with respect to the body (written in the wing frame) is computed as ${}_w\boldsymbol{\omega}^W = \boldsymbol{E}_{wb} \cdot \dot{\boldsymbol{\varphi}}^W$, where $\boldsymbol{E}_{wb}$ is constructed in a similar manner to Eq. (2). The transformation matrix between the body frame and the wing frame is given by $\boldsymbol{T}_{wb}$, which is constructed in a similar manner to Eq. (3)

Finally, the unsteady deformation of each flapping wing is captured by discretizing the structure into one-dimensional beam elements, as seen in Fig. 2. Three displacements and three rotations (as measured in the wing system $x_w - y_w - z_w$) are computed at each finite element node, and a set of element coordinate systems ($x_e - y_e - z_e$) follow each beam finite element as it deforms. The transformation between each of these local systems and the wing system is $\boldsymbol{T}_{ew}$, which may be computed with Rodriguez parameters, as demonstrated by Crisfield (1990).

The relevant metrics of the body motion may be grouped into a state vector $\boldsymbol{q}^B$

$$\boldsymbol{q}^B = \left\{ ({}_i\boldsymbol{r}^B)^T \quad (\boldsymbol{\varphi}^B)^T \quad ({}_b\boldsymbol{v}^B)^T \quad ({}_b\boldsymbol{\omega}^B)^T \right\}^T. \tag{6}$$

There are 12 members of this vector, 6 of which are longitudinal (confined to the $y_b - z_b$ plane in Fig. 1). The structural deformation of each finite element node (three displacements and three rotations), written in the wing coordinate system, may also be grouped into state vectors: $\boldsymbol{u}^R$ and $\boldsymbol{u}^L$ for the right and the left wings, respectively. For longitudinal flight dynamics, each member of $\boldsymbol{u}^R$ will be equal (or equal and opposite) to its counterpart in $\boldsymbol{u}^L$. This work will compute trimmed periodic orbits in the longitudinal plane only, but Floquet multipliers governing lateral dynamics should be retained for a stability analysis. To compute these lateral modes, $\boldsymbol{u}^R$ and $\boldsymbol{u}^L$ need to be considered as separate.
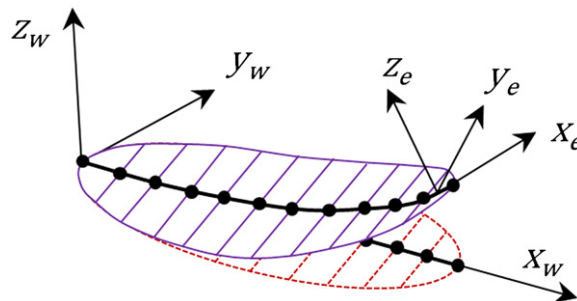

Fig. 2. Deformed and un-deformed wing configurations.

The unsteady motion of the body is governed by the following equation:

$$\begin{bmatrix} \boldsymbol{I} & & & \\ & \boldsymbol{I} & & \\ & & \boldsymbol{I} \cdot m & \\ & & & \boldsymbol{I}_B \end{bmatrix} \cdot \begin{Bmatrix} {}_i\dot{\boldsymbol{r}}^B \\ \dot{\boldsymbol{\varphi}}^B \\ {}_b\dot{\boldsymbol{v}}^B \\ {}_b\dot{\boldsymbol{\omega}}^B \end{Bmatrix} + \begin{bmatrix} \boldsymbol{0} & & & \\ & \boldsymbol{0} & & \\ & & m \cdot {}_b\tilde{\boldsymbol{\omega}}^B & \\ & & & {}_b\tilde{\boldsymbol{\omega}}^B \cdot \boldsymbol{I}_B \end{bmatrix} \cdot \begin{Bmatrix} {}_i\boldsymbol{r}^B \\ \boldsymbol{\varphi}^B \\ {}_b\boldsymbol{v}^B \\ {}_b\boldsymbol{\omega}^B \end{Bmatrix} + \begin{Bmatrix} 0 \\ 0 \\ \boldsymbol{P}_F \\ \boldsymbol{P}_M \end{Bmatrix} = \begin{Bmatrix} \boldsymbol{T}_{bi} \cdot {}_b\boldsymbol{v}^B \\ \boldsymbol{E}_{bi}^{-1} \cdot {}_b\boldsymbol{\omega}^B \\ \boldsymbol{R}_F \\ \boldsymbol{R}_M \end{Bmatrix}, \tag{7}$$

or in more compact form as

$$\boldsymbol{M}^B \cdot \dot{\boldsymbol{q}}^B + \boldsymbol{A}^B \cdot \boldsymbol{q}^B + \boldsymbol{P}^B = \boldsymbol{R}^B, \tag{8}$$

where $\boldsymbol{I}$ is the identity matrix, m is the complete mass of the vehicle (body plus wings), and $\boldsymbol{I}_B$ is the inertia tensor of the body, written in the body coordinate system at point B. The matrix $\boldsymbol{M}^B$ is constant, and the matrix $\boldsymbol{A}^B$ is a function of the body dynamics $\boldsymbol{q}^B$. The force and moment vectors $\boldsymbol{P}^B$ and $\boldsymbol{R}^B$ are highly nonlinear functions of both the body dynamics and the wing structural dynamics. $\boldsymbol{P}_F$ and $\boldsymbol{P}_M$ are the forces and moments about the body's center of gravity due to the inertial loads induced by the flapping wings

$$\boldsymbol{P}_F = \sum_{wings}\{\boldsymbol{P}_{FB}\left(\boldsymbol{q}^B,\dot{\boldsymbol{q}}^B\right) + \boldsymbol{P}_{Fu}\left(\boldsymbol{q}^B,\dot{\boldsymbol{q}}^B\right)\cdot\boldsymbol{u} + \boldsymbol{P}_{F\dot{u}}\left(\boldsymbol{q}^B\right)\cdot\dot{\boldsymbol{u}} + \boldsymbol{P}_{F\ddot{u}}\cdot\ddot{\boldsymbol{u}}\}, \tag{9}$$

$$\boldsymbol{P}_M = \sum_{wings}\left\{\boldsymbol{P}_{MB}\left(\boldsymbol{q}^B,\dot{\boldsymbol{q}}^B\right) + \boldsymbol{P}_{Mu}\left(\boldsymbol{q}^B,\dot{\boldsymbol{q}}^B,\boldsymbol{u}\right)\cdot\boldsymbol{u} + \boldsymbol{P}_{M\dot{u}}\left(\boldsymbol{q}^B,\boldsymbol{u}\right)\cdot\dot{\boldsymbol{u}} + \boldsymbol{P}_{M\ddot{u}}(\boldsymbol{u})\cdot\ddot{\boldsymbol{u}}\right\}, \tag{10}$$

where $\boldsymbol{P}_{FB}$ and $\boldsymbol{P}_{MB}$ reflect the inertial effect of the rigid wings, and the remaining terms are nonlinear couplings between the body's motion and the wing's structural dynamics. The deformation vector $\boldsymbol{u}$ (and its time derivatives) will be either $\boldsymbol{u}^R$ or $\boldsymbol{u}^L$, depending on the wing summation index.

The vectors $\boldsymbol{R}_F$ and $\boldsymbol{R}_M$ are the forces and moments about the body's center of gravity due to aerodynamic loads and gravitational loads

$$\boldsymbol{R}_F = m \cdot {}_b\boldsymbol{g} + \sum_{wings}\left\{\boldsymbol{R}_{Faero}\left(\boldsymbol{q}^B,\dot{\boldsymbol{q}}^B,\boldsymbol{u},\dot{\boldsymbol{u}},\ddot{\boldsymbol{u}}\right)\right\}, \tag{11}$$

$$\boldsymbol{R}_M = \sum_{wings}\left\{\boldsymbol{R}_{Mg}(\boldsymbol{u}) + \boldsymbol{R}_{Maero}\left(\boldsymbol{q}^B,\dot{\boldsymbol{q}}^B,\boldsymbol{u},\dot{\boldsymbol{u}},\ddot{\boldsymbol{u}}\right)\right\}, \tag{12}$$

where ${}_b\boldsymbol{g}$ is the gravitational vector written in the body frame, $\boldsymbol{R}_{Mg}$ are moments about the body's center of gravity due to gravitational forces (where the moment arm depends on the wing's deformation $\boldsymbol{u}$), and $\boldsymbol{R}_{Faero}$ and $\boldsymbol{R}_{Maero}$ are aerodynamic forces and moments, both of which are highly-nonlinear functions of the vehicle's total state. Further details concerning the rigid-wing terms of Eqs. (9)–(12) can be found by Sun et al. (2007) and Stanford et al. (in press), while the terms which include flexible wing motion are detailed by Richter and Patil (2010) and Su and Cesnik (2011).

Though the interactions between flexible wing motion and rigid body motion are captured in a fully nonlinear manner ($\boldsymbol{P}_{Mu}$, for example), the deformation of the wing finite element structure (Fig. 2) is assumed to be governed by linear mechanics in this work. For a given wing, the equations of motion written in the wing frame are

$$\boldsymbol{M}\cdot\ddot{\boldsymbol{u}} + \left(\boldsymbol{C}_{gyr}\left(\boldsymbol{q}^B\right)+\boldsymbol{C}\right)\cdot\dot{\boldsymbol{u}} + \left(\boldsymbol{K}_{dyn}\left(\boldsymbol{q}^B,\dot{\boldsymbol{q}}^B\right)+\boldsymbol{K}\right)\cdot\boldsymbol{u} = \boldsymbol{F}_{iner}\left(\boldsymbol{q}^B,\dot{\boldsymbol{q}}^B\right) + \boldsymbol{F}_{aero}\left(\boldsymbol{q}^B,\dot{\boldsymbol{q}}^B,\boldsymbol{u},\dot{\boldsymbol{u}},\ddot{\boldsymbol{u}}\right). \tag{13}$$

This equation can be written for either the right ($\boldsymbol{u}^R$) or the left ($\boldsymbol{u}^L$) wing, where each term in the matrices and vectors will be equal (or equal and opposite) to its counterpart in the other wing. $\boldsymbol{M}$ is a consistent mass matrix, $\boldsymbol{C}$ is a structural damping matrix (proportional to the mass matrix, for this work), and $\boldsymbol{K}$ is a linear stiffness matrix. $\boldsymbol{C}_{gyr}$ is a skew-symmetric gyroscopic matrix which captures the Coriolis forces, interactions between the deformational velocity $\dot{\boldsymbol{u}}$ and the rotation of the wing frame, which in turn is a function of both the prescribed kinematics as well as the body motion $\boldsymbol{q}^B$. $\boldsymbol{K}_{dyn}$ is a dynamic stiffness matrix which captures the (typically) softening interaction between the rotating frame and the deformation.

The vector $\boldsymbol{F}_{iner}$ is the inertial forces due solely to rigid body motions of the wing frame, and $\boldsymbol{F}_{aero}$ is an aerodynamic force vector. The aerodynamic force vector can be distilled into forces and moments acting at the hinge point H, and transformed into the body frame using $\boldsymbol{T}_{wb}$, in order to compute $\boldsymbol{R}_{Faero}$ and $\boldsymbol{R}_{Maero}$ for Eqs. (11) and (12), respectively (where the moments $\boldsymbol{R}_{Maero}$ must also include the additional moment arm between points B and H in Fig. 1). Aerodynamic effects are captured using the two-dimensional quasi-steady blade element method formulated by Berman and Wang (2007), which will be briefly described here. An airfoil (blade element) is established at each finite element in Fig. 2, and based upon the instantaneous velocity and acceleration of the element (an average of the two nodal values), two aerodynamic forces and one aerodynamic moment is computed in the deformed element coordinate system ($x_e - y_e - z_e$), as seen in Fig. 3

$$\frac{dF_{y_e}}{dx_e} = m_{22}\cdot v_{z_e}\cdot\dot{\psi} - \rho_f\cdot\Gamma\cdot v_{z_e} - m_{11}\cdot a_{y_e} - \frac{dF_{y_e}^v}{dx_e}, \tag{14}$$

$$\frac{dF_{z_e}}{dx_e} = -m_{11}\cdot v_{y_e}\cdot\dot{\psi} + \rho_f\cdot\Gamma\cdot v_{y_e} - m_{22}\cdot a_{z_e} - \frac{dF_{z_e}^v}{dx_e}, \tag{15}$$
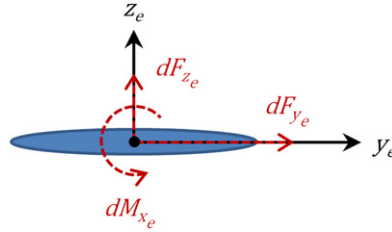
Fig. 3. Blade-element aerodynamic force and moment computations.

$$\frac{dM_{x_e}}{dx_e} = (m_{11} - m_{22}) \cdot v_{y_e} \cdot v_{z_e} - I_a \cdot \ddot{\psi} - \frac{dM_{x_e}^v}{dx_e}. \tag{16}$$

The translational velocities v_{y_e} and v_{z_e}, the axial angular velocity $\dot{\psi}$, the translational accelerations a_{y_e} and a_{z_e}, and the axial angular accelerations $\ddot{\psi}$ represent the total motion of the blade elements (finite elements), written in the deformed element coordinate system. These values reflect the motion of the body ($\boldsymbol{q}^B$, $\dot{\boldsymbol{q}}^B$), the prescribed kinematic motion of the wings ($\boldsymbol{\varphi}^W$), and the subsequent structural deformation of the wings ($\dot{\boldsymbol{u}}$, $\ddot{\boldsymbol{u}}$). ρ_f is the density of the fluid, m_{11}, m_{22}, and I_a are added mass terms, and Γ is the fluid circulation, given by

$$\Gamma = -0.5 \cdot C_T \cdot c \sqrt{v_{y_e}^2 + v_{z_e}^2} \sin(2\alpha) + 0.5 \cdot C_R \cdot c^2 \dot{\psi}, \tag{17}$$

where c is the chord length of the element, C_T and C_R are the translational and rotational force coefficients, and α is the wing section's angle of attack. The viscous terms given above are computed by

$$\frac{d}{dx_e} \begin{Bmatrix} F_{y_e}^v \\ F_{z_e}^v \end{Bmatrix} = 0.5 \cdot \rho_f \cdot c \left(C_D(0) \cdot \cos^2(\alpha) + C_D(\pi/2) \cdot \sin^2(\alpha) \right) \sqrt{v_{y_e}^2 + v_{z_e}^2} \begin{Bmatrix} v_{y_e} \\ v_{z_e} \end{Bmatrix}, \tag{18}$$

$$\frac{dM_{x_e}^v}{dx_e} = \frac{1}{16} \cdot \pi \cdot \rho_f \cdot c^4 \left(\mu_1 \cdot f + \mu_2 \cdot |\dot{\psi}| \right) \dot{\psi}, \tag{19}$$

where C_D is the drag coefficient at angles of attack of 0 and $\pi/2$, μ_1 and μ_2 are dimensionless viscous parameters, and f is the flapping frequency. The aerodynamic force vector of Eq. (13) must be written in the wing frame, and is computed by assembling over each finite element (e)

$$\boldsymbol{F}_{aero} = \sum_e 0.5 L_e \cdot \boldsymbol{T}_{ew}^4 \frac{d}{dx_e} \begin{Bmatrix} 0 & F_{y_e} & F_{z_e} & M_{x_e} & 0 & 0 & 0 & F_{y_e} & F_{z_e} & M_{x_e} & 0 & 0 \end{Bmatrix}^T, \tag{20}$$

where L_e is the length of each finite element, and $\boldsymbol{T}_{ew}^4 = \text{diag}\{\boldsymbol{T}_{ew}, \boldsymbol{T}_{ew}, \boldsymbol{T}_{ew}, \boldsymbol{T}_{ew}\}$, which will be a function of the deformation vector $\boldsymbol{u}$ at each node.

Because the aerodynamic model is quasi-steady rather than unsteady (i.e., the history of the aerodynamics has no explicit effect upon the system), the aerodynamic terms can be expressed as functions of the body dynamics and the wing's structural deformation, via $\boldsymbol{F}_{aero}$, $\boldsymbol{R}_{Faero}$, and $\boldsymbol{R}_{Maero}$. The system behavior is then completely specified by the simultaneous solution of Eq. (8) (for $\boldsymbol{q}^B$) and Eq. (13) (one each for $\boldsymbol{u}^R$ and $\boldsymbol{u}^L$). For unsteady aerodynamics models (such as finite-state inflow representations, vortex shedding methods, or Navier–Stokes solvers), a three-field approach is required. The two-field dynamics problem considered here is efficiently solved by combining the two sets of equations in a monolithic manner

$$\begin{Bmatrix} \dot{\boldsymbol{q}}^B \\ \dot{\boldsymbol{u}}^R \\ \ddot{\boldsymbol{u}}^R \\ \dot{\boldsymbol{u}}^L \\ \ddot{\boldsymbol{u}}^L \end{Bmatrix} = \begin{bmatrix} \boldsymbol{M}^B & & & & \\ & \boldsymbol{I} & & & \\ & & \boldsymbol{M} & & \\ & & & \boldsymbol{I} & \\ & & & & \boldsymbol{M} \end{bmatrix}^{-1} \begin{Bmatrix} \boldsymbol{R}^B - \boldsymbol{P}^B - \boldsymbol{A}^B \cdot \boldsymbol{q}^B \\ \dot{\boldsymbol{u}}^R \\ \boldsymbol{F}_{iner}^R + \boldsymbol{F}_{aero}^R - \left(\boldsymbol{K}_{dyn}^R + \boldsymbol{K} \right) \cdot \boldsymbol{u}^R - \left(\boldsymbol{C}_{gyr}^R + \boldsymbol{C} \right) \cdot \dot{\boldsymbol{u}}^R \\ \dot{\boldsymbol{u}}^L \\ \boldsymbol{F}_{iner}^L + \boldsymbol{F}_{aero}^L - \left(\boldsymbol{K}_{dyn}^L + \boldsymbol{K} \right) \cdot \boldsymbol{u}^L - \left(\boldsymbol{C}_{gyr}^L + \boldsymbol{C} \right) \cdot \dot{\boldsymbol{u}}^L \end{Bmatrix}. \tag{21}$$

Grouping all of the unknowns into a state vector $\boldsymbol{q}$, Eq. (21) can be written compactly as

$$\dot{\boldsymbol{q}} = \boldsymbol{R}(\boldsymbol{q}, \dot{\boldsymbol{q}}). \tag{22}$$

This system of equations is solved with time marching, utilizing a trapezoidal rule for the time derivatives. To account for the strongly-nonlinear dependence of $\boldsymbol{R}$ upon the states $\boldsymbol{q}$ and $\dot{\boldsymbol{q}}$, several Newton–Raphson iterations are conducted within each time step.

Though a direct higher-fidelity analog to Eq. (21) does not, to the best of the to the authors' knowledge, exist in the literature, portions of Eq. (21) have shown adequate comparisons to existing data. The quasi-steady blade element aerodynamic model is presumably of greatest concern (accuracy-wise). The interested reader is referred to Stanford et al. (2012) for a comparison of this model to a high-order Navier–Stokes solver in terms of aerodynamic force generation of a

rigid flapping wing pinned at its root. Stanford et al. (in press) compare flight-dynamic pole-placement (described below) to Navier–Stokes data (from Sun et al. (2007)) for a moving body with two rigid flapping wings, across a range of vehicle scales. Though the comparisons in both of these studies would indicate an acceptable level of accuracy, there is no concrete way of knowing whether the design-optimization studies performed below will push the model outside its range of validity, or whether physical interactions that the optimizer chooses to exploit are low-fidelity artifacts. Clearly, more research is needed in this area.

3. Periodic shooting and Floquet multipliers

For a given set of initial conditions, $\boldsymbol{\eta} = \boldsymbol{q}(0)$, Eq. (22) can be integrated through a single flapping cycle (of period T), and the final state will be $\boldsymbol{q}(T)$. If these two states are equal, then the system is moving through a trimmed periodic orbit. Despite the periodic nature of the prescribed wing kinematics ($\boldsymbol{\varphi}^W$), this will not be the case in general, and so the periodic shooting method is utilized to locate the prescribed initial state $\boldsymbol{\eta}$ that drives the final state $\boldsymbol{q}(T)$ to coincide with $\boldsymbol{\eta}$. The general procedure for nonlinear dynamical systems is described by Nayfeh and Balachandran (1995), and will be briefly described here.

The derivative of $\boldsymbol{q}$ (at any time $t > 0$) with respect to $\boldsymbol{\eta}$ can be computed by time-integrating the equation

$$\frac{\partial}{\partial t}\left(\frac{\partial \boldsymbol{q}}{\partial \boldsymbol{\eta}}\right) = \frac{\partial \dot{\boldsymbol{q}}}{\partial \boldsymbol{\eta}} = \boldsymbol{J} \cdot \frac{\partial \boldsymbol{q}}{\partial \boldsymbol{\eta}} \qquad \frac{\partial \boldsymbol{q}}{\partial \boldsymbol{\eta}}\bigg|_{t=0} = \boldsymbol{I}, \tag{23}$$

where $\boldsymbol{I}$ is the identity matrix, and the Jacobian $\boldsymbol{J}$, referencing the equations of motion (Eq. (22)), is given by

$$\boldsymbol{J} = \left(\boldsymbol{I} - \frac{\partial \boldsymbol{R}}{\partial \dot{\boldsymbol{q}}}\right)^{-1} \cdot \frac{\partial \boldsymbol{R}}{\partial \boldsymbol{q}}. \tag{24}$$

The differential equation for $\partial \boldsymbol{q}/\partial \boldsymbol{\eta}$ is a linear differential equation with time-varying coefficients and multiple right-hand-sides, and may be time-integrated in conjunction with the original equations of motion for $\boldsymbol{q}$ (Eq. (22)). A vector of objective functions may be specified as

$$\boldsymbol{g} = \boldsymbol{q}(T) - \boldsymbol{\eta} = 0. \tag{25}$$

Forcing $\boldsymbol{g} = 0$ would provide a trimmed hovering motion (station-keeping), which is of concern in this work. Different expressions for $\boldsymbol{g}$ are required if trimmed forward-flight is desired (Bierling and Patil, 2009), though this is not considered here. A recurring Newton update loop can be used to locate the initial conditions $\boldsymbol{\eta}$ that satisfy Eq. (25)

$$\left(\frac{\partial \boldsymbol{q}}{\partial \boldsymbol{\eta}}\bigg|_{t=T} - \boldsymbol{I}\right)^n \cdot (\boldsymbol{\eta}^{n+1} - \boldsymbol{\eta}^n) = \boldsymbol{g}^n, \tag{26}$$

where n is the iteration number, which continue until $\boldsymbol{g}^n \to \boldsymbol{0}$. It is understood that a single iteration of Eq. (26) requires time integration through an entire flapping cycle.

The matrix of Eq. (26) is singular, however, due to the fact that prescribing the initial position of the body $_i\boldsymbol{r}^B$ has no impact on the problem. The same orbit will be obtained regardless of where in space the vehicle begins. A remedy suggested by Bierling and Patil (2009) is to replace the two prescribed longitudinal initial conditions ($_iy^B$ and $_iz^B$) with two kinematic variables, grouped into the vector $\boldsymbol{y}$ (which may be a flap phase and amplitude, for example). The two kinematic variables $\boldsymbol{y}$, along with the remaining members of $\boldsymbol{\eta}$, are grouped into a vector of control parameters $\boldsymbol{p}$. It is now desired to locate the vector $\boldsymbol{p}$ such that Eq. (25) is satisfied. Even though the body positions have been removed from the set of control variables, they remain in the definition of $\boldsymbol{g}$: the position at the end of the cycle should coincide with the initial position (which is simply set to zero).

The new recurrence equation is

$$\left(\frac{\partial \boldsymbol{g}}{\partial \boldsymbol{p}}\right)^n \cdot (\boldsymbol{p}^{n+1} - \boldsymbol{p}^n) = \boldsymbol{g}^n. \tag{27}$$

The majority of the matrix in Eq. (27) is composed of $\partial \boldsymbol{q}/\partial \boldsymbol{\eta}$, but the derivative $\partial \boldsymbol{q}/\partial \boldsymbol{y}$ is now needed as well. This term can be computed by differentiating the equations of motion with respect to the control variables $\boldsymbol{y}$

$$\frac{\partial}{\partial t}\left(\frac{\partial \boldsymbol{q}}{\partial \boldsymbol{y}}\right) = \frac{\partial \dot{\boldsymbol{q}}}{\partial \boldsymbol{y}} = \frac{\partial \boldsymbol{R}}{\partial \boldsymbol{y}} + \frac{\partial \boldsymbol{R}}{\partial \boldsymbol{q}} \cdot \frac{\partial \boldsymbol{q}}{\partial \boldsymbol{y}} + \frac{\partial \boldsymbol{R}}{\partial \dot{\boldsymbol{q}}} \cdot \frac{\partial \dot{\boldsymbol{q}}}{\partial \boldsymbol{y}}, \tag{28}$$

$$\left(\boldsymbol{I} - \frac{\partial \boldsymbol{R}}{\partial \dot{\boldsymbol{q}}}\right) \cdot \frac{\partial}{\partial t}\left(\frac{\partial \boldsymbol{q}}{\partial \boldsymbol{y}}\right) - \frac{\partial \boldsymbol{R}}{\partial \boldsymbol{q}} \cdot \frac{\partial \boldsymbol{q}}{\partial \boldsymbol{y}} = \frac{\partial \boldsymbol{R}}{\partial \boldsymbol{y}} \qquad \frac{\partial \boldsymbol{q}}{\partial \boldsymbol{y}}\bigg|_{t=0} = 0. \tag{29}$$

Like $\partial \boldsymbol{q}/\partial \boldsymbol{\eta}$, this linear set of ordinary differential equations for $\partial \boldsymbol{q}/\partial \boldsymbol{y}$ may be computed forward in time, in conjunction with $\boldsymbol{q}$, and it has two right hand sides, which is the size of $\boldsymbol{y}$. As $\boldsymbol{y}$ is a collection of parameters, the explicit residual derivative $\partial \boldsymbol{R}/\partial \boldsymbol{y}$ is a known quantity. The value of $\partial \boldsymbol{q}/\partial \boldsymbol{y}$ at the final time step ($t = T$) can be used to populate $\partial \boldsymbol{g}/\partial \boldsymbol{p}$.

Once Eq. (27) has converged ($\boldsymbol{g} \rightarrow \boldsymbol{0}$), a trimmed periodic orbit of the system has been located, and the monodromy matrix (Nayfeh and Balachandran, 1995), or state transition matrix (Johnson, 1980) is defined as

$$\boldsymbol{\Phi} = \frac{\partial \boldsymbol{q}}{\partial \boldsymbol{\eta}}\Bigg|_{t=T}. \tag{30}$$

The eigenvalues Λ_i of this matrix are the Floquet multipliers, and the characteristic exponents are defined as $\lambda_i = \ln(\Lambda_i)/T$. The periodic system is stable if each Λ_i is located within the unit circle (i.e., the real parts of each λ_i are negative).

4. Parameterization and optimization

The deforming flapping wing structure seen in Fig. 2 is discretized into N equal-length beam finite elements. Each element plays two simultaneous roles: it acts as the structural cross-section, as well as the airfoil of each aerodynamic blade element (in contrast with scenarios where a beam-like spar constitutes structural reinforcement for a larger wing surface, as in Isogai and Harino (2007)). The dimensions of each rectangular element cross-section can be varied independently, as seen in Fig. 4. The chord length of each element, c_i, acts as both the aerodynamic chord for the blade element method (namely Eqs. (17)–(19)), as well as the width of the beam structure, and will thus have a strong inertial and stiffness impact. The thickness of each element, h_i, will slightly alter the aerodynamic forces (via the added mass terms m_{11}, m_{22}, and I_a), and will also have a significant effect upon the wing's mass and stiffness. These dependencies are explicit; the coupled nature of the aeroelastic flight dynamics solver will ensure that both chord and thickness distribution affect each term in Eq. (21) in an implicit manner.

The kinematic flapping motions are assumed to be of the form (Berman and Wang, 2007)

$$\phi^W = \frac{\phi_m}{\sin^{-1}(K_\phi)} \sin^{-1}\left(K_\phi \sin(2\pi f t)\right) + \phi_o,$$

$$\theta^W = \theta_m \cos(2\pi f t + \theta_s) + \theta_o,$$

$$\eta^W = \frac{\eta_m}{\tanh(C_\eta)} \tanh\left(C_\eta \sin(2\pi f t + \eta_s)\right) + \eta_o. \tag{31}$$

The parameter K_ϕ may vary between 0 (sinusoidal waveform) and 1 (triangular waveform), while the parameter C_η varies between 0 (sinusoidal waveform) and ∞ (step function). Not including the frequency f, ten parameters describe the three flapping angles in Eq. (31) as a function of time. Two of these parameters must be set aside for the periodic shooting method

$$\boldsymbol{y} = \left\{ \phi_m \quad \phi_o \right\}. \tag{32}$$

The amplitude and offset of the azimuthal stroke plane motion provides the shooting method with enough authority to force a trimmed orbit ($\boldsymbol{g} = \boldsymbol{0}$), a choice made by Richter and Patil (2010) and Bierling and Patil (2009) also.

The remaining 8 kinematic parameters not used in $\boldsymbol{y}$ are set as design variables, which may be grouped with the chord and thickness variables to form the final design vector

$$\boldsymbol{x} = \left\{ c_1 \quad c_2 \quad \cdots \quad c_N \quad h_1 \quad h_2 \quad \cdots \quad h_N \quad K_\phi \quad \theta_m \quad \theta_s \quad \theta_o \quad \eta_m \quad \eta_s \quad \eta_o \quad C_\eta \right\}. \tag{33}$$

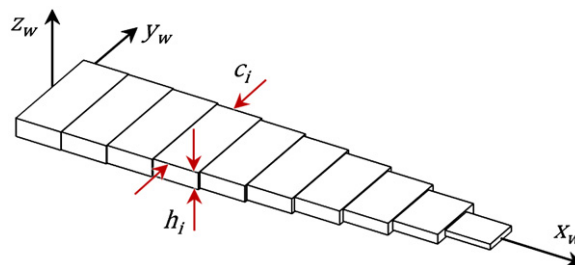The baseline, lower bounds, and upper bounds of these design variables are given in Table 1.

Fig. 4. Chord length and thickness of each finite element along the beam-wing.

Table 1
Baseline values and side constraints for each design variable.

	c_i (mm)	h_i (mm)	K_ϕ (dimensionless)	θ_m (rad)	θ_s (rad)	θ_o (rad)	η_m (rad)	η_s (rad)	η_o (rad)	C_η (dimensionless)
Min.	10	0.2	0.01	$-\pi/4$	$-\pi/2$	$-\pi/4$	$-\pi/2$	$-\pi/2$	$-\pi/2$	0.01
Baseline	25	0.6	0.01	0	0	0	$\pi/4$	$\pi/2$	$-\pi/2$	0.1
Max.	60	2.5	0.99	$\pi/4$	$\pi/2$	$\pi/4$	$\pi/2$	$\pi/2$	$\pi/2$	4

Two optimization problems are considered here. The first attempts to push each Floquet multiplier towards the unit circle, using a bound formulation

$$\min_{\boldsymbol{x},\,\beta} \; \beta$$

$$\text{s.t. :} \begin{cases} ||A_i|| \leq \beta & i=1,\ldots,n, \\ \delta_{tip}(t) \leq \delta^*, \\ w_{tip}(t) \leq w^*, \\ \sigma(t) \leq \sigma^*, \\ \boldsymbol{x}_{min} \leq \boldsymbol{x} \leq \boldsymbol{x}_{max}, \end{cases} \tag{34}$$

where the bound β is both an objective function and a design variable. If β decreases below unity in a feasible manner, then the system achieves open-loop stability. The second constraint stipulates that the minimum separation distance between the left and the right wing tip always be larger than some threshold δ^*. Aerodynamic physics that govern wing–wing interactions and wing–body interactions (i.e., clap-fling) have not been included in the analysis, and so maintaining a separation of δ^* should preserve the accuracy of the method. Similarly, the third constraint requires that the out-of-plane structural tip deflection (as measured in the local wing frame) remain less than w^*, in order to minimize the geometric structural nonlinearities (which have not been included either).

The fourth constraint of Eq. (34) requires that the elastic Von-Mises stresses that develop throughout the wing structure remain less than some allowable value, and the fifth constraint requires that the design variables lie between the side constraints given in Table 1. A second optimization problem minimizes the peak power required to actuate both wings, with no regard to the Floquet multipliers

$$\min_{\boldsymbol{x}} \; \max(p(t))$$

$$\text{s.t. :} \begin{cases} \delta_{tip}(t) \leq \delta^*, \\ w_{tip}(t) \leq w^*, \\ \sigma(t) \leq \sigma^*, \\ \boldsymbol{x}_{min} \leq \boldsymbol{x} \leq \boldsymbol{x}_{max}. \end{cases} \tag{35}$$

The power requirements are given by the following equation:

$$p = dK_E/dt + dS_E/dt + p_{aero}. \tag{36}$$

where K_E is the kinetic energy of the wing (due to both rigid body and deformational motions), S_E is the strain energy of the beam (due only to deformational motions), and p_{aero} is the aerodynamic power.

Both optimization problems (34) and (35) are solved using gradient-based optimization via the method of moving asymptotes (Svanberg, 1987), with design gradients of the objectives and constraints computed using finite difference approximations. Analytically-computed derivatives of Floquet multipliers can be obtained (see Stanford et al. (in press), for rigid flapping wings), but the method becomes less tractable for larger systems. This is because the monodromy matrix $\boldsymbol{\Phi}$ is itself a derivative (of the final state with respect to the initial state), and so design derivatives of this matrix, required for the Floquet multiplier derivatives, necessitate second derivatives of the system (e.g., $\partial^2 \boldsymbol{R}/\partial \boldsymbol{q}^2$). For smaller systems, these higher-derivatives can be computed using finite differences over the vector $\boldsymbol{q}$; if all required first derivatives are computed analytically, the process can be labeled "semi-analytical" (Shih et al., 1996). Obviously, this process is not feasible for high-dimensional state vectors.

5. Results

For this work, a single flapping cycle is broken into 100 time steps, and Eqs. (22), (23), and (29) are integrated in time using a trapezoidal rule. The periodic shooting method will typically converge (using under-relaxation of Eq. (27)) within 5–20 iterations, depending on the initial guess. The body has an ellipsoidal shape, with a major axis of 0.07 m and a minor axis of 0.014 m. Two flexible flapping wings are attached to this body, each with a length of 10 cm. Each wing is discretized into 10 beam elements (N), resulting in 28 possible design variables (Eq. (33)), though subsets of the design vector $\boldsymbol{x}$ are explored below. The remaining parameters are given in Table 2, where $_b\boldsymbol{r}_{BH}$ is the distance from the body's center

Table 2
Geometric, inertial, and elastic properties of the flapping vehicle.

Parameter	Value	Parameter	Value
$_b\boldsymbol{r}^{BH}$	$\{\pm 0.015\ 0.03\ 0\}$ m	f	200 rad/s
m_{body}	0.01 kg	ρ_f	1.225 kg/m³
$\boldsymbol{I}_B(1,1)$	1.6987×10^{-5} kg m²	C_T	1.83
$\boldsymbol{I}_B(2,2)$	1.3067×10^{-6} kg m²	$C_D(0)$	0.21
$\boldsymbol{I}_B(3,3)$	1.6987×10^{-5} kg m²	$C_D(\pi/2)$	3.35
N	10	C_R	π
Wing length	10 cm	μ_1	0.2
Elastic modulus	70 GPa	μ_2	0
Shear modulus	26.9 GPa	σ^*	350 MPa
Wing density	1000 kg/m³	W^*	2 cm
$\boldsymbol{C}$	$20 \cdot \boldsymbol{M}$	δ^*	4 cm
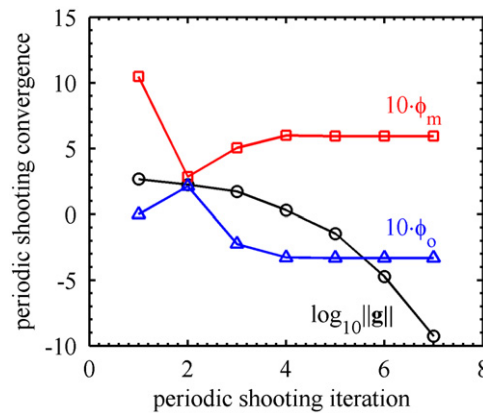
Fig. 5. Convergence of the periodic shooting method for the baseline design.

of gravity to each hinge point, measured in the body frame (B to H in Fig. 1), and m_{body} is the mass of the elliptical body. The total mass of the system, m in Eq. (7), is the sum of m_{body} and the mass of the two wings, where the latter is computed from the chord c_i and thickness h_i distribution along the span.

Focusing first on the baseline parameters of Table 1, the convergence of the periodic shooting method is given in Fig. 5. Eq. (27) converges in 7 iterations, when the norm of $\boldsymbol{g}$ (Eq. (25)) decreases to 10^{-9}. The two kinematic control parameters grouped into the vector $\boldsymbol{y}$ (ϕ_m and ϕ_o) are also shown at each iteration. These are only two of many control parameters in $\boldsymbol{p}$ used to enforce time-periodicity; the initial conditions of the body and wing deformation, $\boldsymbol{\eta}$, are not shown here. Each member of the initial guess $\boldsymbol{p}^0$ is set to zero except ϕ_m, which is set to $\pi/3$ rad. In order to trim the vehicle, the amplitude of this azimuthal stroke motion is decreased to 0.593 rad, and the offset ϕ_o is dropped to -0.332. The mean stroke motion is therefore biased towards the rear of the vehicle.

Additional details concerning the convergence to time-periodicity are given in Fig. 6, which shows the longitudinal body position and attitude (lateral terms are zero, as the flapping is symmetric), and the out-of-plane wing tip deflection w_{tip}. These are plotted as a function of the azimuthal flapping stroke motion ϕ^W, at selected iterations of Fig. 5. It is noted that the range of this flapping motion changes at each iteration, via the amplitude and phase information in Fig. 5. During the first iteration, each plotted system degree of freedom, and its first time derivative, begins at 0 when $t=0$. This is because $\boldsymbol{\eta}$ is set to zero, as noted above. The system state at the end of the flapping cycle ($t=T$) is very different from the initial state. The body has drifted forward ($_i y^B$) by 2.45 cm, upwards ($_i z^B$) by 0.24 cm, and is pitched up (Ψ^B) by 16.1°. The structural tip deflection, on the other hand, is nearly time-periodic, but the deformational velocity ($\dot{w}_{tip}$), is not.

The second iteration of the periodic shooting method is distinctly different from the first, and if under-relaxation is not used (a factor of 0.8) during these initial iterations, the process will diverge. The dynamic behavior of the third iteration finally shows some similarity with the final, converged periodic orbit. During this periodic motion, the body oscillates about the origin through a small orbit, consistently pitched up. The final wing deformation is much smaller than in the first iteration, with an amplitude of 13.3% of the wing length L. Peak deflection occurs near stroke reversal, which is typically due to the inertial load vector $\boldsymbol{F}_{iner}$ (Stanford et al., 2012). The deflection hysteresis loop between the downstroke and the upstroke is related to the damping, either structural ($\boldsymbol{C}$) or aerodynamic ($\boldsymbol{F}_{aero}$).
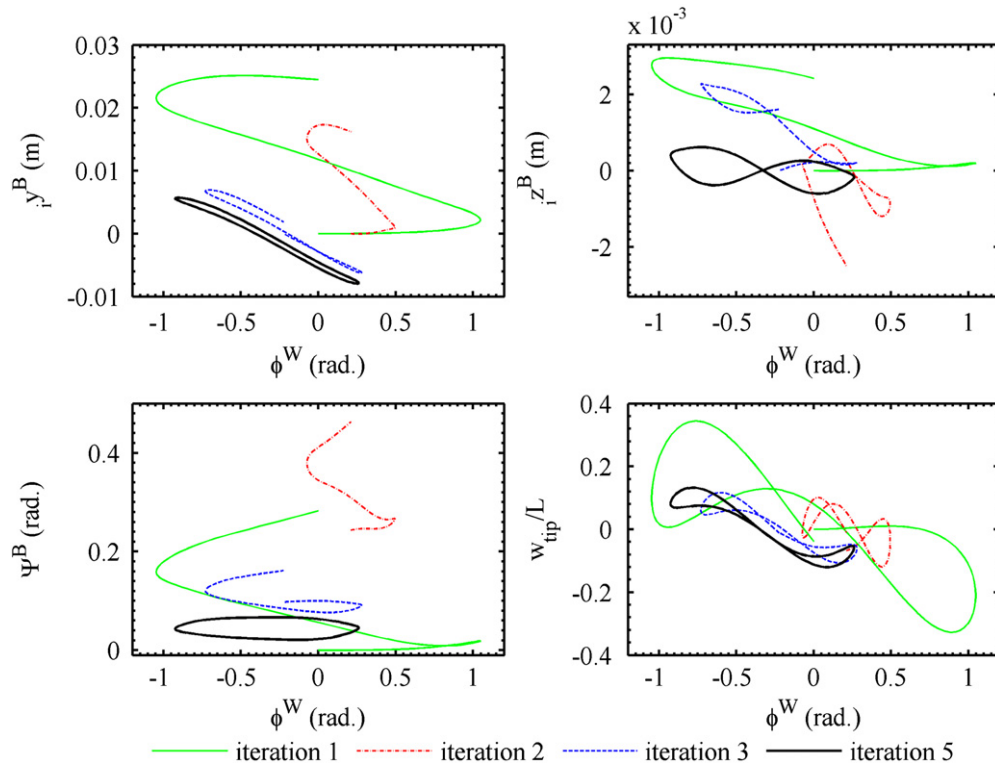
Fig. 6. Body position ($_iy_B$, $_iz_B$), attitude (Ψ^B), and out-of-plane wing tip deformation (w_{tip}) as a function of the azimuthal flapping stroke motion ϕ^W, at selected iterations during the shooting method.
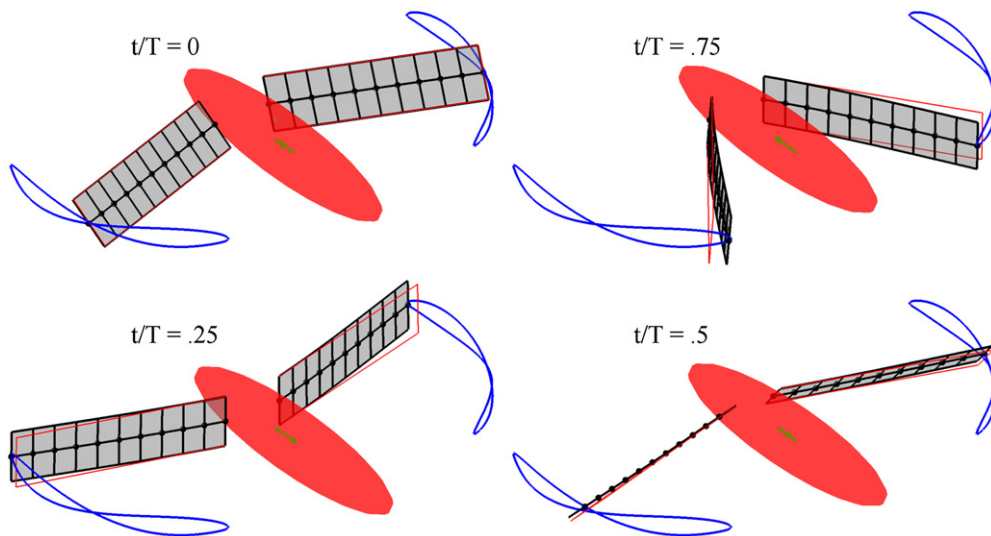

Fig. 7. Four snapshots of the time-periodic baseline vehicle dynamics.

Additional information pertaining to the time-periodic dynamics of the system is given in Figs. 7 and 8. The former shows four snapshots of the vehicle motion, with the wing tip and the body's center of gravity traced out through the orbit. The motion of a fictional rigid wing is also shown, to highlight the differences between the commanded wing motion (via the root kinematics) and the actual motion of the flexible wing. These differences are also noted in Fig. 8, which shows the motion of both wing tip sections. It should be emphasized that the wing is not actually rigid; if it were, the periodic shooting method would converge to a different orbit. Furthermore, Fig. 8 shows the absolute motion of the wing, rather than the motion of the wing relative to the body.
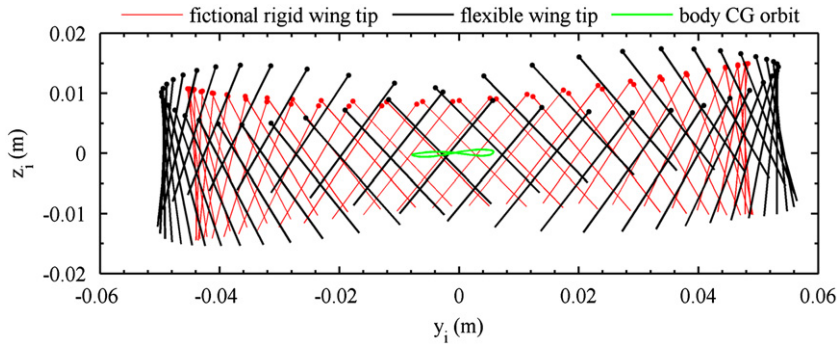
Fig. 8. Time-periodic wing tip motion and body motion of the baseline vehicle.
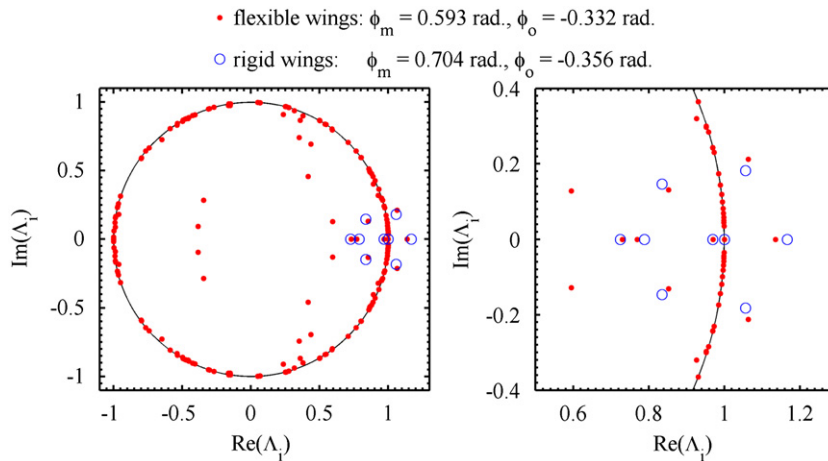

Fig. 9. Floquet multipliers of the baseline time-periodic system, as well as a vehicle with rigid wings.

Except for ϕ_m and ϕ_o, the kinematics for the baseline case are as indicated in Table 1, with the out-of-stroke plane deviation θ^W set to zero. Despite this, the stroke plane of Fig. 8 is clearly pitched up, which is due to the attitude of the vehicle seen in Fig. 6. The flexible wing is also traveling through a figure-8 motion, which is due in small part to a similar path traveled by the body (whose path is also seen in Fig. 8), and in larger part to the passive deflection of the wing. The effective stroke of the flexible wing is wider than the fictional rigid wing, which would indicate (and is confirmed below), that a vehicle outfitted with rigid wings would require a larger stroke amplitude ϕ_m to achieve a trimmed state, and thus expend more power.

The Floquet multipliers Λ_i of this trimmed periodic system are given in Fig. 9, along with multipliers for the periodic dynamics of a vehicle with rigid wings. Unlike the fictional rigid wing data of the previous two figures, the rigid data in Fig. 9 is from an entirely separate periodic shooting analysis. The kinematic control parameters are listed above the figure, where the stroke amplitude needed to trim the rigid system is 18.0% higher than for the flexible system, as expected. The three multipliers associated with the body position ($_ix^B$, $_iy^B$, and $_iz^B$) are always equal to unity, for the same reason that these terms cannot be used to control the periodic shooting method. Perturbing the initial position of the vehicle's orbit by some δ will just cause the final state to be shifted by this same amount: the fundamental dynamics remain unchanged.

The remaining eight multipliers dominated by the body motion (as opposed to flexible wing motion) can be directly compared with their rigid counterparts, where the advent of flexibility has improved the stability of the subsidence critical mode, from 1.167 down to 1.136. This is a lateral mode, whereas the next two largest modes (whose stability has decreased with flexibility) are oscillatory longitudinal modes. As the largest Floquet multipliers lie outside the unit circle, the trimmed periodic orbit of this baseline design is unstable, and perturbations from the orbit will amplify over time. The remaining multipliers of the flexible system are all stable for this case, though instabilities of the flexible wing deformation are in some cases possible (Rosenfeld and Wereley, 2009). Many eigenvalues lie very close to the unit circle, which represent high-frequency vibration modes of the beam structures, which are lightly damped. If stiffness-proportional damping had been used for this work (rather than mass-proportionality), the multipliers of the strongly-damped higher modes would tend towards zero.

Table 3
Stability and peak power consumption of the six optimal designs.

Case	Design variables	Optimization	Max ($\|\Lambda_i\|$)	Max ($p(t)$)
Baseline	–	–	1.136	1306 W/kg
1a	c_i and h_i	Eq. (34)	**1.045**	2189 W/kg
1b	c_i and h_i	Eq. (35)	1.146	**204.4 W/kg**
2a	Kinematics	Eq. (34)	**0.987**	1411 W/kg
2b	Kinematics	Eq. (35)	1.081	**698.8 W/kg**
3a	c_i, h_i, and kinematics	Eq. (34)	**0.978**	1307 W/kg
3b	c_i, h_i, and kinematics	Eq. (35)	1.106	**78.51 W/kg**

Table 4
Kinematic parameters of the six optimal designs.

| Case	Control variables		Design variables							
	ϕ_m (rad)	ϕ_o (rad)	K_ϕ (dimensionless)	θ_m (rad)	θ_s (rad)	θ_o (rad)	η_m (rad)	η_s (rad)	η_o (rad)	C_η (dimensionless)
Baseline	0.593	−0.332	0.010	0	0	0	$\pi/4$	$\pi/2$	$-\pi/2$	0.100
1a	0.851	−0.374	0.010	0	0	0	$\pi/4$	$\pi/2$	$-\pi/2$	0.100
1b	0.333	−0.371	0.010	0	0	0	$\pi/4$	$\pi/2$	$-\pi/2$	0.100
2a	0.638	−0.656	0.037	−0.105	0.175	0.614	0.656	1.107	−1.267	0.252
2b	0.493	−0.383	0.131	−0.011	−0.088	−0.201	0.749	1.385	−0.945	3.219
3a	0.633	−0.754	0.035	−0.204	0.220	0.522	0.682	1.073	−1.517	0.254
3b	0.224	−0.387	0.121	−0.005	−0.094	0.184	0.901	1.517	−1.207	0.402
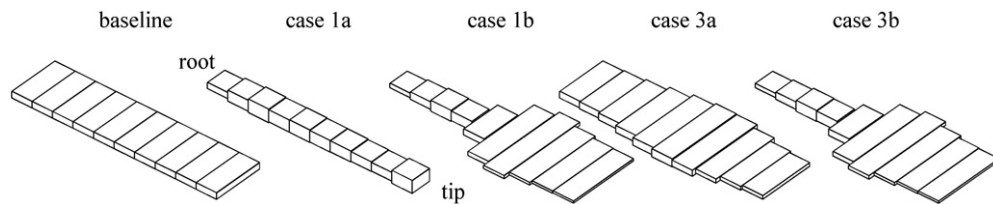
Fig. 10. Optimal chord and thickness distributions along the wing: thickness is scaled by a factor of 5.

Having assessed the behavior of the baseline design, attention is now turned to design optimization. Six optimal cases are presented here. The first two consider only chord c_i and thickness h_i variables to minimize the Floquet multipliers (Eq. (34)) or the peak power (Eq. (35)). The second two solve these problems only using the kinematic design variables, and the final two utilize the entire variable vector $\boldsymbol{x}$ of Eq. (33). The performance of these six optimal designs is given in Table 3, the kinematic motions for each design in Table 4, and the chord and thickness distributions are drawn in Fig. 10 (where the thicknesses are scaled by a factor of five).

Several observations can be made from this data. Providing the optimizer with more design variables (case 3 as opposed to cases 1 or 2) improves the performance metrics, in that lower peak power consumption and more stable vehicles may be obtained. Generally, chord and thickness variables are more successful at decreasing power (i.e., case 1b) than decreasing the Floquet multipliers (case 1a), and the opposite is true for the kinematic variables (cases 2a and 2b). It should be noted, however, that though cases 1a and 1b have no explicit design control over the kinematics, they do implicitly control ϕ_m and ϕ_o in order to trim the vehicle. Case 1a drops each chord variable c_i to its lower bound (10 cm), and thus the azimuthal stroke amplitude must be increased to 0.851 rad in order to achieve a periodic orbit. Case 1b, on the other hand, can decrease the power requirement by decreasing the stroke amplitude to 0.333 rad, and therefore must increase the wing chord towards the tip (where the velocities will be highest) to generate enough aerodynamic lift for trim.

These trade-offs are not available to the optimizer when only kinematics are provided in cases 2a and 2b, and so other design strategies must be used. Stability is improved (case 2a) by shifting the azimuthal stroke motion towards the rear of the vehicle ($\phi_o = -0.656$ rad), and providing a moderate amount of out-of-stroke plane deviation θ^W which is out of phase with ϕ^W (such that the wing tip travels in a loop). The power-optimal design of case 2b is defined by large values of C_η, where the snap-like rotation at the ends of each stroke correspond to a sharp drop in aerodynamic power.

The periodic dynamics of case 3a are seen in Fig. 11, where chord, thickness, and kinematic variables are all used to improve the stability. The kinematic variables for this design are very similar to the design of case 2a, though the magnitudes of both ϕ_o and θ_m are larger. The rearward shift of the flapping motion (ϕ_o) and the looped path of the wing tip (θ_m) are clearly seen in the figure. The wing's chord and thickness distribution are very different from the corresponding
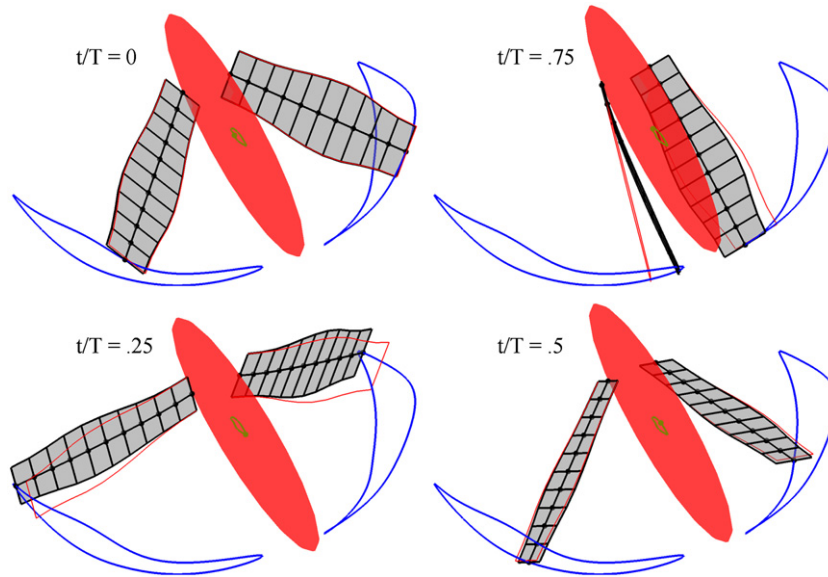
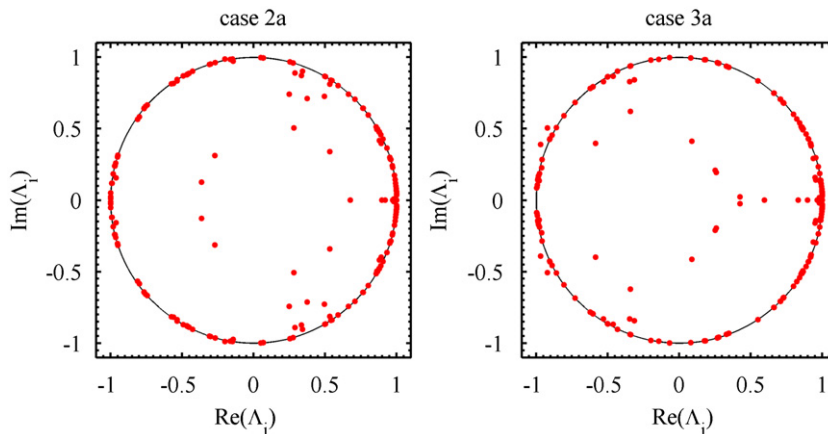Fig. 11. Four snapshots of the time-periodic vehicle dynamics for case 3a.

Fig. 12. Floquet multipliers of the optimal time-periodic systems of case 2a and case 3a.

case 1a, however, where the wing is much thinner, has a larger aspect ratio, and the local chord is largest at mid-span. Due in part to the large rearward shift of the kinematics, and in part to the large out-of-plane structural deformations (at least compared to the baseline data of Fig. 7: the w_{tip} constraint is active), the tips of the left and right wing come in close proximity to each other, and to the body. The δ_{tip} constraint is active for this case.

This relationship between wing proximity and stability has also been noted by Stanford et al. (in press), and decreasing the allowable δ^* will presumably push the critical Floquet multiplier farther inside the unit circle. The blade-element aerodynamic tool used here is incapable of correctly capturing these interactions, however. The stress constraint σ is inactive for this and every case considered in this work. This is due to the fact that the tip deflection constraint is a reasonable surrogate for the elastic stresses, and the former constraint boundary is more conservative than the latter. Replacing the linear beam model with a nonlinear model would allow the w_{tip} constraint to be removed from the problem definition, and then the stress constraint is expected to become active, as seen in Stanford et al. (2012).

It can also be seen in Fig. 11 that the body of the vehicle is pitched up (Ψ^B) throughout the periodic orbit by roughly 45°, which is much larger than the baseline design (Fig. 7) or any of the power-optimal designs. A similar body attitude is utilized by case 2a; the Floquet multipliers of both cases are given in Fig. 12. Two significant challenges are inherent in these optimal solutions to Eq. (34) via the bound method. The first is the fact that some Floquet multipliers permanently reside on the unit circle (or very close to it), and therefore should not be included in the optimization problem. Therefore, the eigenvectors of each multiplier are scanned to find modes with substantial rigid-body motion. Eight such multipliers are then retained for the constraint $\Lambda_i \leq \beta$, as a vehicle with rigid wings would have 8 relevant modes.

The second problem is mode-switching: improving the stability of a critical Floquet multiplier will typically cause another multiplier to destabilize, and the identity of the critical mode will switch. This presents a discontinuity in the design space, impeding the convergence of the gradient-based optimizer. As such, it seems likely that superior designs to cases 2a and 3a exist in the design space, but could not be located with the tools utilized here. Non-gradient-based optimizers may be considered, but these methods may struggle with the periodic shooting method. For the gradient-based approach used here, the initial guess for the orbit control vector $\boldsymbol{p}^0$ (Eq. (27)) is set equal to the converged vector from the previous design iterate. If $\boldsymbol{p}^0$ is instead re-initialized to a vector of zeros, the shooting method can diverge, particularly for highly-optimal designs. A non-gradient-based optimizer has no logical choice for an initial guess $\boldsymbol{p}^0$.

Despite these issues, the largest Floquet multiplier of the eight modes dominated by rigid-body motion has been pushed into the unit circle. For case 2a, the largest Λ_i is 0.987, and so this vehicle is stable in an open loop sense. As with the baseline vehicle in Fig. 9, many multipliers associated with the flexible wing dynamics lie directly on the unit circle in Fig. 12. Because the multipliers associated with the body motion ($_ix^B$, $_iy^B$, and $_iz^B$) are still equal to unity, this vehicle is longitudinally and laterally stable but cannot hold a fixed hovering position in the presence of a disturbance, as will be seen below. Closed-loop feedback control is needed for station-keeping (Oppenheimer et al., 2010).

Including all of the chord, thickness, and kinematic design variables in case 3a decreases the largest Λ_i of the eight rigid-body modes to 0.978 (Fig. 12). This vehicle is also (in theory) open loop stable, with stronger damping back to the trimmed orbit in the presence of disturbances than case 2a. The Floquet multipliers predict a linear stability, an outcome which is exactly realized for very small disturbances (Nayfeh and Balachandran, 1995). Nonlinearities induced by larger disturbances to the trimmed orbit can still cause unstable motion, but the lower Floquet multiplier in case 3a (as opposed to case 2a) should provide a greater robustness with regards to this effect. However, it can be seen in Fig. 12 that a high-frequency mode (associated with wing torsion) has inadvertently moved outside the unit circle during the case 3a optimization process. This design is still linearly unstable therefore, the ramifications of which are discussed below.

The problem of unstable flexible wing modes may be remedied by including all of the Floquet multipliers in the bound constraint of Eq. (34). This substantial increase in the number of eigenvalue constraints severely complicated both the mode-switching and the mode-identification issues described above, and for this work, prevented any conclusive convergence of the optimization process. Additional work is needed to clarify and solve these issues.

The trimmed periodic motion of case 3b is seen in Fig. 13. The overall shape of the wing is very similar to that of case 1b, as are many of the design trends. A low stroke amplitude ($\phi_m = 0.224$ rad, the smallest of any seen in Table 4) drops the required inertial power, but the large out-board wing chord, as well as the substantial deformational velocity due to the inertial tip snap, provides enough aerodynamic lift to satisfy trim requirements. The power requirements are also decreased by the very low thickness at the wing tip (Fig. 10), which will drop the rotational moment of inertia. The commanded stroke-deviation θ^W is very small for this case, but the same passive wing deformation provides the final wing motion with a strong figure-8 pattern. It is finally noted that the body motion for this case is much smaller than the previous examples, presumably due to the small movement of the wings and the forces/moments they impart on the body. For this case then, linearizing the dynamics about a fixed point (zero body movement), and evaluating the resulting eigenvalues may give very similar modes to the nonlinear orbit-based process used here (comparisons between the two methods are discussed by Bierling and Patil (2009)).

The peak power for this case is two orders of magnitude less than the power requirements of the baseline design, but the expected tradeoff with stability is evident, where the largest Floquet multiplier of case 3b lies well outside the unit
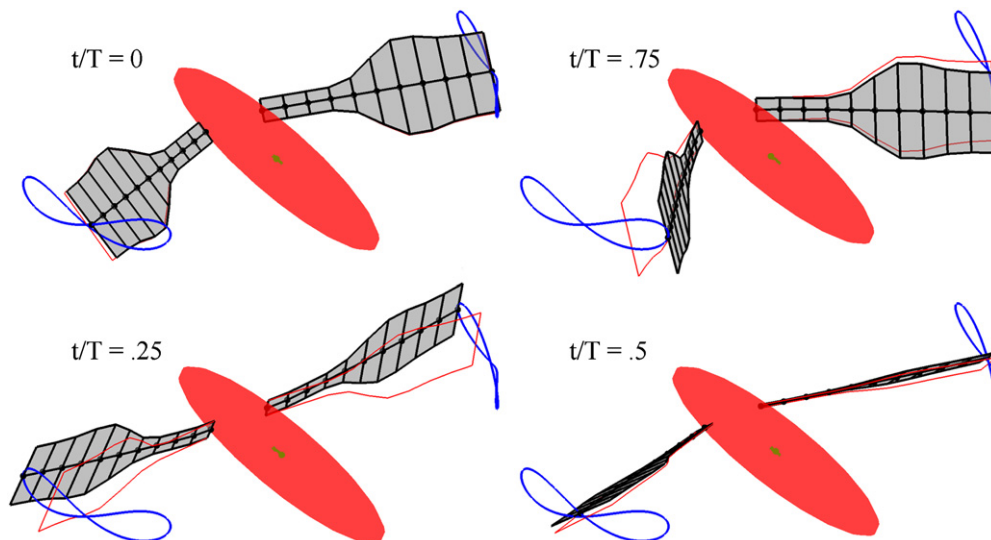

Fig. 13. Four snapshots of the time-periodic vehicle dynamics for case 3b.

circle. Additional details of the power consumption for these two cases are given in Fig. 14, where power is normalized by the mass of the body, and is broken out into components listed in Eq. (36). The kinetic energy rate dK_E/dt is broken into a rigid portion (associated with the kinematics of the fictional rigid wings) and a flexible portion ($\dot{\boldsymbol{u}}^R \cdot \boldsymbol{M} \cdot \ddot{\boldsymbol{u}}^R + \dot{\boldsymbol{u}}^L \cdot \boldsymbol{M} \cdot \ddot{\boldsymbol{u}}^L$), where the former is the main contributor for the baseline vehicle. The elastic portion of dK_E/dt and the strain energy rate ($\dot{\boldsymbol{u}}^R \cdot \boldsymbol{K} \cdot \boldsymbol{u}^R + \dot{\boldsymbol{u}}^L \cdot \boldsymbol{K} \cdot \boldsymbol{u}^L$) nearly cancel one another, as may be inferred from the deformational equations of motion (Eq. (13)), termed "reactance cancelation" by Tantanawat and Kota (2007).

The aerodynamic power of the baseline design is largely positive, with peaks at t/T near 0.5 and 1, which corresponds to moments of high wingtip velocity in Fig. 7. Contrastingly, the aerodynamic power of the optimal case 3b is the dominant term, and has substantial negative values. This negative aerodynamic power is due to rapid rotation of the wings at stroke reversal, via the relatively large value of $C_\eta = 0.402$ (these trends are exploited even more by case 2b, where $C_\eta = 3.219$). Peaks in aerodynamic power are offset by near-simultaneous drops in the flexible portion of dK_E/dt, and in dS_E/dt, termed 'generative-load exploitation' by Tantanawat and Kota (2007). These energy trade-offs keep the peak values of the total power p well below the largest of any individual power term, and it is these peak total values which are exposed to the optimizer in Eq. (35).

If a long-time simulation is performed for the system dynamics of Eq. (22), and the initial conditions ($\boldsymbol{\eta}$) and the kinematic controls ($\boldsymbol{y}$) are set equal to the values found in the trimmed control vector $\boldsymbol{p}$, then the system state will return to $\boldsymbol{\eta}$ at the end of each flapping cycle. If the system is unstable, then numerical round-off errors will eventually destabilize this recurrence. Regardless of the stability, if the initial conditions are perturbed by some vector $\overline{\boldsymbol{\eta}}$, then the state error at the end of the Nth flapping cycle is (Nayfeh and Balachandran, 1995)

$$\boldsymbol{e}_N = \boldsymbol{q}(NT) - \boldsymbol{\eta} = \boldsymbol{\Phi}^N \cdot \overline{\boldsymbol{\eta}}. \tag{37}$$

Clearly, the eigenvalues of the monodromy matrix $\boldsymbol{\Phi}$ (Floquet multipliers) dictate whether the error $\boldsymbol{e}$ decays to zero (at which point the dynamics return to the trimmed orbit) or amplifies. Furthermore, $\boldsymbol{e}_N$ is only a linearized trend (albeit about a fully nonlinear orbit): long-time marching of the system is required to assess whether or not nonlinearities destabilize the system.

This exercise is conducted in Figs. 15 and 16 for the optimal case 3a, where a perturbation is applied to the initial body pitch angle Ψ^B only: the remaining members of $\overline{\boldsymbol{\eta}}$ are zero. The left side of Fig. 15 plots the pitch angle as a function of time
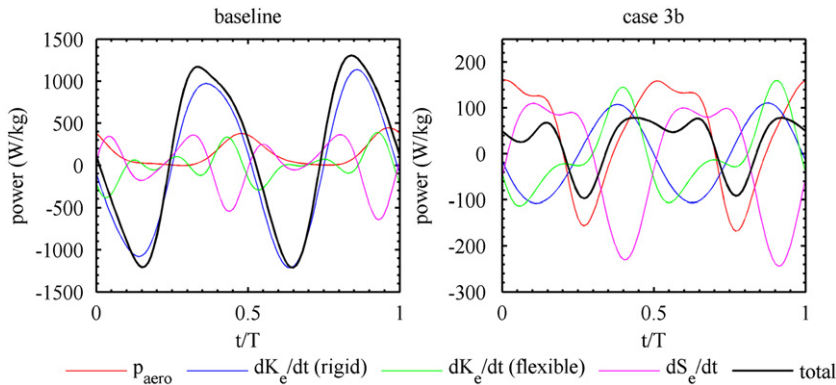

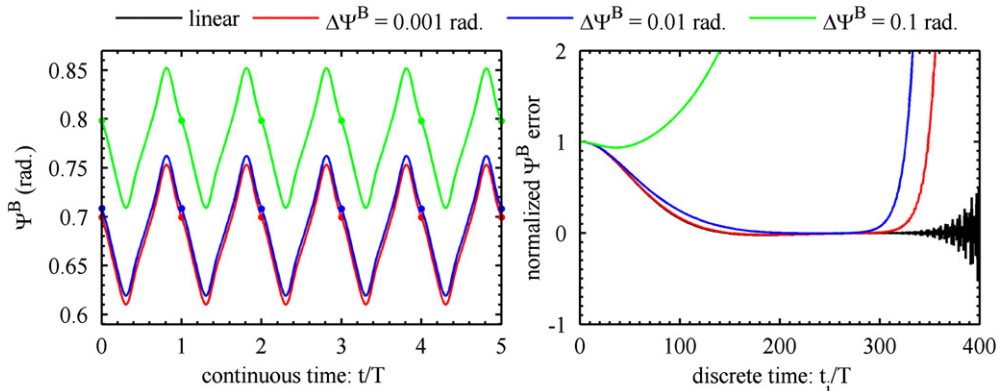Fig. 14. Input power requirements for the baseline design and the optimal design case 3b.

Fig. 15. Case 3a pitch dynamics in response to an initial perturbation from the trimmed pitch angle.
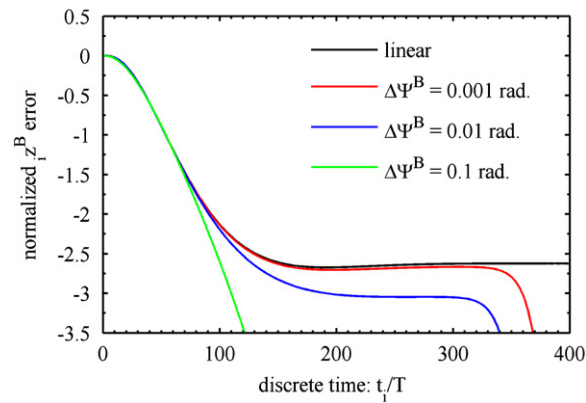
Fig. 16. Case 3a position dynamics in response to an initial perturbation from the trimmed pitch angle.

through five flapping cycles, for three perturbation values. The right side provides the normalized error in discrete time through 400 flapping cycles: the pitch angle is sampled at the end of each cycle, compared to the trimmed pitch angle, and then normalized by the perturbation value. Each of these normalized errors in discrete time begins at unity, and deviations from the linearized prediction of Eq. (37) are indicative of nonlinear effects.

The linearized error e_N is slightly under-damped, and decreases to zero within 250 flapping cycles. After 300 cycles, a high-frequency unstable oscillation is noted. The former effect is due to the fact that all of the Floquet multipliers with substantial rigid-body content are within the unit circle, while the latter is because a high-frequency flexible mode is outside this circle, as seen in Fig. 12. Smaller initial perturbations (0.001 and 0.01 rad) closely follow the initially-stable trends of the linearized model, but then sharply diverge after 300 flapping cycles. Presumably, this is due to nonlinear interactions between the unstable torsional wing mode and the body dynamics. Larger perturbations (0.1 rad) cause the system to diverge almost immediately. Though not shown here, the long-time dynamics of case 2a to a small perturbation are stable, as all of the pertinent Floquet multiplier lie within the unit circle (Fig. 12).

Additional discrete-time results for case 3a are given in Fig. 16 for the body's vertical position ($_iz^B$) error in response to the same initial pitch perturbations. These errors all start at 0, as the perturbation is solely applied to pitch. The linearized position error does not settle back to zero, but rather to some negative value. This is as discussed above: the Floquet multiplier associated with $_iz^B$ is equal to unity, and so the open-loop system has no way of forcing this metric back to its original value: closed-loop control is required. Fully-nonlinear simulations with small pitch perturbations destabilize after 300 flapping cycles, while larger perturbations destabilize much sooner, behavior similar to that of Fig. 15.

6. Conclusions

This paper has developed a framework for analyzing the time-periodic flight and structural dynamics of a small vehicle with two flexible flapping wings. The kinematics of the wings are prescribed, but the subsequent beam-like passive deformation of the wings, and the nonlinear motion of the body due to the inertial and aerodynamic wing loading, is not. This strongly coupled system is assembled into a two-field monolithic system of equations, where the quasi-steady blade element aerodynamic states are projected onto the wing deformation and body dynamic states. Periodic orbits of this system are computed with a periodic shooting method, where the initial conditions of the system are identified such that the final state converges to this initial state. This process is facilitated with the state transition matrix, as well as replacing two of the position initial conditions with two kinematic control parameters.

The final system is then exposed to a gradient-based optimizer, in order to solve six optimization problems: minimize the largest flight mechanics eigenvalue (Floquet multiplier) of the system for improved stability, or minimize the peak power draw during the cycle, for shape/structure variables, kinematic variables, or both. Design derivatives of the objectives and constraints are found using finite differencing. In general, kinematic variables have greater leverage at improving the stability, where all the Floquet multipliers can be pushed within the unit circle. Open-loop stability can be obtained, but closed-loop control is still needed for station-keeping in the presence of a disturbance, or for maintaining stability in the presence of large disturbances. Chord and thickness variables are more adept at decreasing power requirements, but both metrics are further improved by including the entire suite of available design variables.

Acknowledgments

References

Berman, G., Wang, Z., 2007. Energy-minimizing kinematics in hovering insect flight. Journal of Fluid Mechanics 582, 153–168.

Bierling, T., Patil, M., 2009. Nonlinear Dynamics and Stability of Flapping-wing Flight. International Forum on Aeroelasticity and Structural Dynamics, Seattle, WA, June 2–5.

Bolender, M., 2010. Open-loop stability of flapping flight in hover. In: AIAA Guidance, Navigation, and Control Conference, Toronto, Canada, August 2–5.

Celi, R., 1999. Recent applications of design optimization to rotorcraft: a survey. Journal of Aircraft 36, 176–189.

Crisfield, M., 1990. A consistent co-rotational formulation for non-linear, three-dimensional, beam-elements. Computer Methods in Applied Mechanics and Engineering 81, 131–150.

Dietl, J., Garcia, E., 2008. Stability in ornithopter longitudinal flight dynamics. Journal of Guidance, Control, and Dynamics 31, 1157–1162.

Isogai, K., Harino, Y., 2007. Optimum aeroelastic design of a flapping wing. Journal of Aircraft 44, 2040–2048.

Johnson, W., 1980. Helicopter Theory. Princeton University Press.

Nayfeh, A., Balachandran, B., 1995. Applied Nonlinear Dynamics. John Wiley and Sons, New York.

Oppenheimer, M., Doman, D., Sigthorsson, D., 2010. Dynamics and control of a biomimetic vehicle using biased wingbeat forcing functions. Journal of Guidance, Control, and Dynamics 34, 204–217.

Orlowski, C., Girard, A., 2011. Modeling and simulation of nonlinear dynamics of flapping wing micro air vehicles. AIAA Journal 49, 969–981.

Richter, M., Patil, M., 2010. Influence of wing flexibility on the stability of flapping flight. In: AIAA Atmospheric Flight Mechanics Conference, Toronto, Canada, August 2–5.

Rosenfeld, N., Wereley, N., 2009. Time-periodic stability of a flapping insect wing structure in hover. Journal of Aircraft 46, 450–464.

Seyranian, A., Solem, F., Pedersen, P., 2000. Multi-parameter linear periodic systems: sensitivity analysis and applications. Journal of Sound and Vibration 229, 89–111.

Shih, I., Spence, A., Celi, R., 1996. Semianalytical sensitivity of floquet characteristic exponents with application to rotary-wing aeroelasticity. Journal of Aircraft 33, 322–330.

Stanford, B., Kurdi, M., Beran, P., McClung, A., 2012. Shape, structure, and kinematic parameterization of a power-optimal wing. Journal of Aircraft 49, 1687–1699.

Stanford, B., Beran, P., Patil, M. Using floquet multiplier sensitivities to assess performance trade-offs in flapping wing flight dynamics. Journal of Guidance, Control, and Dynamics, in press.

Su, W., Cesnik, C., 2011. Flight dynamic stability of a flapping wing micro air vehicle in hover. In: AIAA Structures, Structural Dynamics, and Materials Conference, Denver, CO, April 4–7.

Sun, M., Wang, J., Xiong, Y., 2007. Dynamic flight stability of hovering insects. Acta Mechanica Sinica 23, 231–246.

Svanberg, K., 1987. The method of moving asymptotes—a new method for structural optimization. International Journal for Numerical Methods in Engineering 24, 359–373.

Tantanawat, T., Kota, S., 2007. Design of compliant mechanisms for minimizing input power in dynamic applications. Journal of Mechanical Design 129, 1064–1075.

Wu, P., Ifju, P., Stanford, B., 2010. Flapping wing structural deformation and thrust correlation study with flexible membrane wings. AIAA Journal 48, 2111–2121.